Research Article

Nano Research
2022, 15(7): 6678–6685

ISSN 1998-0124 CN 11-5974/O4
https://doi.org/10.1007/s12274-022-4226-5

Hard nanocrystalline gold materials prepared via high-pressure phase transformation

Chenlong Xie[1], Wenxin Niu[2,3], Penghui Li[1], Yiyao Ge[4], Jiawei Liu[2], Zhanxi Fan[4,5,6], Xiaoxiao Liu[1], Ye Chen[7], Ming Zhou[2], Zihe Li[1], Mengdong Ma[1], Yonghai Yue[8], Jing Wang[9], Li Zhu[1], Kun Luo[1], Yang Zhang[1], Yingju Wu[1], Lin Wang[1], Bo Xu[1], Hua Zhang[4,5,6] (✉), Zhisheng Zhao[1] (✉), and Yongjun Tian[1] (✉)

[1] *Center for High Pressure Science (CHiPS), State Key Laboratory of Metastable Materials Science and Technology, Yanshan University, Qinhuangdao 066004, China*
[2] *Center for Programmable Materials, School of Materials Science and Engineering, Nanyang Technological University, Singapore 639798, Singapore*
[3] *State Key Laboratory of Electroanalytical Chemistry, Changchun Institute of Applied Chemistry, Chinese Academy of Sciences, Changchun 130022, China*
[4] *Department of Chemistry, City University of Hong Kong, Hong Kong, China*
[5] *Hong Kong Branch of National Precious Metals Material Engineering Research Center (NPMM), City University of Hong Kong, Hong Kong, China*
[6] *Shenzhen Research Institute, City University of Hong Kong, Shenzhen 518057, China*
[7] *Department of Chemistry, The Chinese University of Hong Kong, Hong Kong, China*
[8] *School of Chemistry, Beijing Advanced Innovation Center for Biomedical Engineering, Beihang University, Beijing 100190, China*
[9] *Institute of Mechanics, Chinese Academy of Sciences, Beijing 100190, China*

Received: 10 February 2022 / **Accepted:** 10 February 2022

ABSTRACT

As one of the important materials, nanocrystalline Au (n-Au) has gained numerous interests in recent decades owing to its unique properties and promising applications. However, most of the current n-Au thin films are supported on substrates, limiting the study on their mechanical properties and applications. Therefore, it is urgently desired to develop a new strategy to prepare n-Au materials with superior mechanical strength and hardness. Here, a hard n-Au material with an average grain size of ~ 40 nm is prepared by cold-forging of the unique Au nanoribbons (NRBs) with unconventional 4H phase under high pressure. Systematic characterizations reveal the phase transformation from 4H to face-centered cubic (fcc) phase during the cold compression. Impressively, the compressive yield strength and Vickers hardness (H_V) of the prepared n-Au material reach ~ 140.2 MPa and ~ 1.0 GPa, which are 4.2 and 2.2 times of the microcrystalline Au foil, respectively. This work demonstrates that the combination of high-pressure cold-forging and the *in-situ* 4H-to-fcc phase transformation can effectively inhibit the grain growth in the obtained n-Au materials, leading to the formation of novel hard n-Au materials. Our strategy opens up a new avenue for the preparation of nanocrystalline metals with superior mechanical property.

KEYWORDS

nanocrystalline Au, high hardness, high strength, high-pressure forging, 4H Au nanoribbons

1 Introduction

Rationally tuning the structural parameters of polycrystalline metals, such as grain size, morphology, and grain boundary, can efficiently regulate their mechanical properties [1, 2]. In particular, nanocrystalline metals normally with an average grain size of less than 100 nm could exhibit superior mechanical properties, e.g., high yield strength, hardness, and wear resistance, compared with their microcrystalline counterparts, showing great potentials in a wide range of applications [3–6]. To date, various synthetic strategies have been developed to prepare nanocrystalline metals, such as powder metallurgy techniques [7], equal channel angular extrusion [8], and electrodeposition [9]. However, by using these methods, it still remains difficult to achieve the precise structural engineering of nanocrystalline metals with small and grain sizes for boosting the application performance. Taking Au as a typical example, although nanocrystalline Au (n-Au) films could be prepared on specific substrates by gas deposition [10–12] and electroplating method [13], they usually possess limited thickness and their architectures strongly depend on the substrates. Moreover, the as-formed Au films on the substrates are difficult to be stripped or transferred for other applications. Therefore, it is imperative to develop new and effective strategies to prepare freestanding n-Au materials with excellent mechanical strength and hardness for future applications.

Previous studies have proven that the high-pressure-assisted synthesis is a promising method to prepare ultra-hard materials, such as the nanotwinned cubic boron nitride (BN) [14] and nanotwinned diamond [15]. In particular, the structure of starting materials used for the high-pressure synthesis has been demonstrated to play a key role in determining the final structure and the property of as-prepared materials. For instance,

Address correspondence to Hua Zhang, hua.zhang@cityu.edu.hk; Zhisheng Zhao, zzhao@ysu.edu.cn; Yongjun Tian, fhcl@ysu.edu.cn

turbostratic onion-like BN nanoparticles (NPs) and onion-like carbon NPs are essential starting materials for the synthesis of ultra-hard nanotwinned cubic BN [14] and nanotwinned diamond [15], respectively. As known, Au nanomaterials with distinct structures have been prepared and extensively studied [16–21], which can also be used as starting materials in the high-pressure forging fabrication. In particular, with the rapid development of phase engineering of nanomaterials (PEN) [22–26], Au nanomaterials with unconventional crystal phases including 4H-phase Au nanoribbons (NRBs) and 2H-phase Au nanosheets [27, 28], which are different from the thermodynamically stable face-centered cubic (fcc) Au, have been synthesized [17]. However, the preparation of n-Au via high-pressure cold-forging of Au nanocrystals with unconventional phases has been rarely reported.

In this work, the n-Au materials with a grain size of ~ 40 nm are prepared by cold-forging of 4H Au NRBs under high pressure. It is found that the combination of high-pressure cold-forging and the *in-situ* 4H-to-fcc phase transformation effectively inhibits the grain growth in the obtained n-Au, and thus enables the preparation of n-Au materials with nanoscale grain size (Fig. 1). Impressively, the prepared n-Au materials possess a high yield strength of ~ 140.2 MPa and a high Vickers hardness (H_V) of ~ 1.0 GPa, which are 4.2 and 2.2 times of microcrystalline Au foil, respectively. The nanoscale grain strengthening in accordance with the Hall–Petch relationship endows the as-synthesized n-Au materials with excellent hardness, which is better than most reported Au materials. The high-pressure forging of unconventional-phase nanocrystals opens an avenue for the rational fabrication of nanocrystalline metals with exceptional mechanical properties for future applications.

2 Experimental section

2.1 Chemicals

Au(III) chloride hydrate ($HAuCl_4$, ~ 50% Au basis), oleylamine ($C_{18}H_{37}N$, 70%), 1,2-dichloropropane ($C_3H_6Cl_2$, 99%), chloroform ($CHCl_3$, 99%), hexane (C_6H_{14}, 99%), acetone (C_3H_6O, 99.5%), and other chemicals without being specially mentioned were all purchased from Sigma-Aldrich. All the chemicals were used as received without further purification. The micro-polycrystalline fcc Au foil with high purity (~ 99.9975%) was purchased from Alfa Aesar.

2.2 Sample preparation

The 4H Au NRBs were synthesized according to our previous report [27]. In a typical synthesis, $HAuCl_4$ (4.08 mg) and oleylamine (220 μL) were dissolved in the mixture of hexane (3.54 mL) and 1,2-dichloropropane (250 μL) in a 20 mL glass bottle. Subsequently, the glass bottle was capped and heated in an oven at 58 °C for 16 h. The resulting products were collected by centrifugation (5,000 rpm, 3 min), washed at least three times with chloroform, and then dried in vacuum for 12 h. The obtained Au NRBs were first pre-compressed, and then compressed using a pair of diamond anvils with 300-μm-diameter culets and Re as a gasket. No pressure medium was used during the compression. After decompression, the obtained n-Au materials were taken from the chamber, and then used for the mechanical measurements.

As comparison, other Au compacts were also prepared by compressing the fcc Au NPs and Au foil via the aforementioned compression process used for preparing the n-Au materials. The fcc Au NPs were synthesized by using a previously reported method with slight modification [29]. Briefly, 12 mg of $HAuCl_4{\cdot}3H_2O$, 5 mL of chloroform, and 1 mL of oleylamine were added into a 20-mL glass vial at room temperature. After agitation for 2 min using vortex, the resultant pale-yellow solution was heated to 60 °C and maintained for 4 h in an oil bath under magnetic stirring, followed by natural cooling down to the room temperature. Subsequently, 5 mL of acetone was added into the aforementioned solution, which was then centrifuged at 12,000 rpm for 10 min and washed twice with hexane at 12,000 rpm for 10 min. Finally, the as-obtained product was re-dispersed in 5 mL of hexane. The dry fcc Au NPs were obtained by evaporation of hexane for the future usage.

2.3 High-pressure *in-situ* X-ray diffraction (XRD) measurements

Symmetric-type diamond anvil cells (DAC) with 300-μm-diameter culets were used in synchrotron XRD measurements. The Re gasket was pre-indented to a thickness of ~ 30 μm, and then a hole with a diameter of 100 μm was drilled in the center which served as the sample chamber during compression. To reveal the phase transformation of 4H Au NRBs and the equation of state (EOS) under hydrostatic pressure, the silicone oil was used as the pressure transmitting medium during compression. In addition, in order to prepare samples used for mechanical measurements, 4H Au NRBs were also compressed without using pressure medium, and the corresponding *in-situ* XRD data during such non-hydrostatic process were also recorded. The pressure within a DAC was calibrated according to the pressure-dependent shift of the standard ruby fluorescence peak [30]. The *in-situ* XRD measurements were performed at hard X-ray micro-focusing beamline BL15U1 at Shanghai Synchrotron Radiation Facility and 4W2 High-pressure Station of Beijing Synchrotron Radiation Facility with X-ray wavelength of 0.6199 Å. The CeO_2 powder was used as the standard sample to perform the calibration of geometry parameters. The two-dimensional (2D) image plate patterns were integrated to one-dimensional (1D) patterns by using the Fit2D software [31]. The resulting diffraction patterns were fitted via the Rietveld refinement with the GSAS-II software [32].

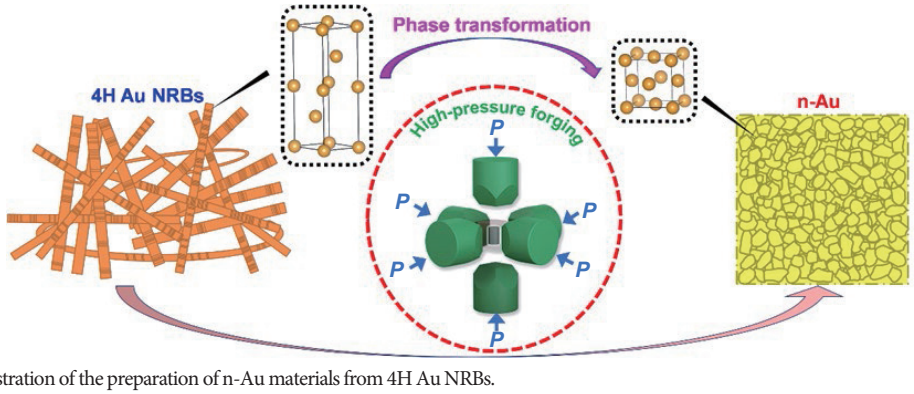

Figure 1 Schematic illustration of the preparation of n-Au materials from 4H Au NRBs.

2.4 Sample characterizations

Au samples were characterized on the transmission electron microscopy (TEM) (Talos F200X, Thermo Fisher Scientific) with an accelerating voltage of 200 kV. To prepare the TEM samples, thin slices were fabricated by focused ion beam (FIB) milling (Scios, FEI) under the voltage of 30 kV. For the high-resolution TEM (HRTEM) characterization, the prepared slices were thinned under the voltage of 5 kV and current of 16 pA for 10 min. The indentations on the sample surface were characterized by using the scanning electron microscopy (SEM) (Scio 1, Thermo Fisher Scientific) under the voltage of 20 kV and current of 0.4 nA in back-scattered electron (BSE) imaging mode.

2.5 Hardness measurements

The H_V of Au samples was measured by two methods, i.e., microhardness test (KB 5 BVZ) with a standard square-pyramidal diamond indenter and nanoindentation test (Key-sight Nano Indenter G200) with a three-sided pyramidal Berkovich diamond indenter. The applied load in microhardness tests was 196 mN, and both the loading time and dwell time were 20 s. H_V was determined based on the equation of $H_V = 1{,}854.4\ F/L^2$, where F is the applied load in Newton and L is the mean length of two diagonals of the indentation in micrometers. The hardness of each Au sample was tested at 5 different positions. During the nanoindentation test, the continuous stiffness measurement (CSM) was carried out and the indenter parameters were first calibrated against hard materials in a wide hardness range, including SiO_2, Al_2O_3, and SiC.

2.6 Micro-pillar compression testing

The Au micro-columns with a diameter of ~ 4 μm and aspect ratio of ~ 1.5 were prepared using the FIB equipment (Scios, FEI). Briefly, under the voltage of 30 kV and current of 30 nA, an Au sample was first carved to obtain circular crater (20 μm in diameter) and micro-column (~ 8 μm in diameter). Then, the micro-column was beam-milled under the voltage of 30 kV and current of 300 pA to obtain the micro-column with the diameter size of ~ 6 μm. Under the voltage of 30 kV and current of 100 pA, the micro-column was further beam-milled to decrease its diameter to ~ 5 μm. In order to minimize the surface damage, the micro-column was beam-milled under the voltage of 30 kV and low current of 30 pA to obtain the expected diameter size, i.e., ~ 4 μm. The micro-compression measurements were performed at PI 85SEM pico-indenter (Hysitron) equipped with a flattened tip (R = 5 μm) by the displacement/loading control.

3 Results and discussion

3.1 Characterization of 4H Au NRBs

The Au NRBs with the unconventional 4H phase, referred to as 4H Au NRBs, were synthesized using our previously reported method [27]. As shown in the TEM image (Fig. S1(a) in the Electronic Supplementary Material (ESM)), the length and width of synthesized 4H Au NRBs were from hundreds of nanometers to several micrometers and 36.2 ± 13.0 nm (Fig. S1(b) in the ESM), respectively. The HRTEM image and the corresponding fast Fourier transform (FFT) pattern reveal the exposure of (110) plane in the 4H Au NRBs (Fig. S1(c) in the ESM), and the atomic stacking mode of "ABCBABCB" can be clearly observed in the high-magnification HRTEM image (Fig. S1(d) in the ESM). Since the 4H phase is a metastable phase of Au, it can be transformed into the thermodynamically stable fcc phase at high pressure [33] or elevated temperature [34].

3.2 Phase transformation of 4H Au NRBs under high-pressure forging

The synthesized 4H Au NRBs were used for the high-pressure cold-forging. In this work, two different high-pressure loadings, i.e., non-hydrostatic and hydrostatic conditions, were applied. Specifically, the non-hydrostatic high-pressure experiment aimed to prepare a series of n-Au materials with different phase ratios under different pressures, which were further used for the mechanical property study. The hydrostatic high-pressure experiment was conducted to further confirm the *in-situ* phase transformation process of 4H Au NRBs under high pressure and also to determine the EOS of 4H Au.

High-pressure *in-situ* XRD measurement was carried out in a DAC in order to investigate the phase evolution of the 4H Au under pressure. It is worth mentioning that weak diffraction peaks assigned to fcc Au were observed in the starting materials in both non-hydrostatic and hydrostatic *in-situ* XRD patterns, arising from the very small amount of by-products (i.e., fcc Au NPs) obtained during the synthesis of 4H Au NRBs (Fig. S1(a) in the ESM) [27]. Under the non-hydrostatic condition, all diffraction peaks shifted to higher angles with the continuous increase of pressure (Fig. 2(a)), indicating the pressure-induced lattice shrinkage of Au. The sudden drop of the diffraction peak area ratio of $(102)_{4H}/(200)_{fcc}$ at a low non-hydrostatic pressure of 4.0 GPa (Fig. 2(b)) shows that the substantial 4H-to-fcc phase transformation of Au occurred. With the further increase of pressure from 4.0 to 21.6 GPa, the diffraction peak intensities of 4H Au further decreased while those of fcc Au gradually increased (Fig. 2(a)). When the pressure reached 21.6 GPa, the diffraction peak area ratio of $(102)_{4H}/(200)_{fcc}$ decreased to zero (Fig. 2(b)), indicating that the 4H-to-fcc phase transformation of Au was completed. Moreover, only diffraction peaks corresponding to fcc Au could be observed after releasing the pressure (Fig. 2(a)), indicating that such 4H-to-fcc phase transformation was irreversible. Figure 2(c) exhibits the optical image of the n-Au material obtained by cold-forging of 4H Au NRBs at 21.6 GPa under non-hydrostatic condition, showing the normal color of fcc Au.

Similarly, under the hydrostatic condition (Fig. S2(a) in the ESM), the 4H phase of Au NRBs could also irreversibly transform to the fcc phase, which was maintained after releasing the pressure to ambient pressure. As shown in Fig. S2(a) in the ESM, in the low hydrostatic pressure range of 0–3.2 GPa, the 4H phase of Au was maintained, and it started to transform to the fcc phase when the pressure exceeded 3.2 GPa, as confirmed by the sudden drop of the diffraction peak area ratio of $(102)_{4H}/(200)_{fcc}$ shown in Fig. S2(b) in the ESM. At 28.6 GPa, the diffraction peak area ratio of $(102)_{4H}/(200)_{fcc}$ decreased to almost zero, indicating 4H-to-fcc phase transformation of Au was completed (Figs. S2(a) and S2(b) in the ESM). Furthermore, the *in-situ* XRD results under the hydrostatic pressure condition (Fig. S2(a) in the ESM) were used to calculate the accurate EOS of 4H Au (Fig. S2(c) in the ESM). Through the Rietveld refinement of the corresponding XRD patterns (Fig. S3 in the ESM), the unit cell volume change of 4H Au NRBs under pressure was determined (Fig. S2(c) in the ESM). Then the EOS of 4H Au was fitted according to the Birch–Murnaghan third-order EOS (Eq. (1)) [35]

$$P = \frac{3}{2}B_0 \times \left[(V_0/V)^{\frac{7}{3}} - (V_0/V)^{\frac{5}{3}}\right] \times \left\{1 - \frac{3}{4}\left(4 - B_0'\right) \times \left[(V_0/V)^{\frac{2}{3}} - 1\right]\right\} \quad (1)$$

where P is the pressure, V is the volume at pressure P, V_0 is the volume at zero pressure, and B_0 and B_0' are the bulk modulus and

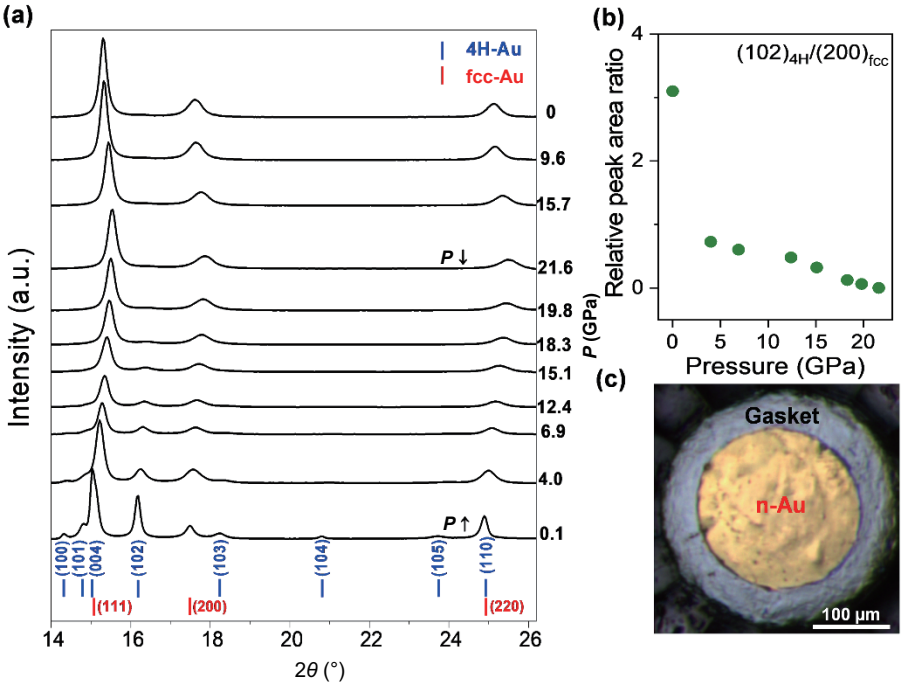

Figure 2 (a) *In-situ* XRD patterns obtained at different pressures from 0.1 to 21.6 GPa under non-hydrostatic condition. No transmitting medium is used during the compression. The blue and red bars represent the standard diffraction peak positions of 4H and fcc Au at ambient pressure, respectively. (b) The peak area ratios of $(102)_{4H}/(200)_{fcc}$ as a function of pressure. (c) The optical image of the prepared n-Au sample obtained by cold-forging of 4H Au NRBs at 21.6 GPa.

its first pressure derivative, respectively. The obtained results were $B_0 = 80.9 \pm 4.5$ GPa and $B_0' = 17.2 \pm 2.1$. Compared with the fcc Au with an experimental value of $B_0 = 167$ GPa [36], the 4H Au possessed a much smaller B_0 value, indicating that the 4H Au was more sensitive to the high-pressure compression as compared with the fcc Au.

3.3 Characterization of as-prepared n-Au materials

In order to study the structural evolution of 4H Au NRBs during the non-hydrostatic compression process, a series of n-Au samples prepared at different pressures, i.e., 2.7 (Figs. 3(a)–3(c)), 8.5 (Fig. S4 in the ESM), and 29.8 GPa (Figs. 3(d)–3(f)), were characterized. The dark field TEM image of the obtained n-Au material prepared at 2.7 GPa (denoted as n-Au-2.7 GPa) is shown in Fig. 3(a). The HRTEM image (Fig. 3(b)) and selected area electron diffraction (SAED) pattern (Fig. 3(c)) of n-Au-2.7 GPa confirm its mixed 4H/fcc phase. The co-existence of two different atomic stacking modes, i.e., "ABCABC" in fcc phase and "ABCBABCB" in 4H phase (inset in Fig. 3(b)), demonstrates the occurrence of 4H-to-fcc phase transformation at 2.7 GPa. When the compression pressure was further increased to 8.5 GPa, the 4H domains could still be observed in the obtained n-Au sample (denoted as n-Au-8.5 GPa, Fig. S4 in the ESM), indicating the incomplete 4H-to-fcc phase transformation. When compressing the 4H Au NRBs at a high pressure of 29.8 GPa, the obtained n-Au material (Fig. 3(d)), denoted as n-Au-29.8 GPa, exhibited a pure fcc phase, which was demonstrated by the presence of $(1\bar{1}1)_{fcc}$ and $(\bar{1}11)_{fcc}$ crystal plane with an interplanar distance of 2.35 Å (Fig. 3(e) and the inset) and the SAED pattern (Fig. 3(f)), indicating the complete 4H-to-fcc phase transformation at such a high pressure. It is worth mentioning that the obtained n-Au-2.7 GPa, n-Au-8.5 GPa, and n-Au-29.8 GPa all possessed a grain size of ~ 40 nm (Table 1).

For comparison, we also prepared the Au compacts through high-pressure forging of other Au materials, i.e., fcc Au NPs with a size of 64.7 ± 26.8 nm (Fig. S5(a) in the ESM and Table 1) and the commercial microcrystalline fcc Au foil (Fig. S5(b) in the ESM and Table 1). As shown in Fig. 3(g), the Au compact prepared from the fcc Au NPs at 28.2 GPa, denoted as AuNPs-compact-28.2 GPa, was composed of elliptical crystalline grains with average length and width of 183.9 ± 54.7 and 96.6 ± 37.0 nm, respectively (Table 1). The HRTEM images (Fig. 3(h) and the inset) and SAED pattern (Fig. 3(i)) clearly show the lattice distance of 2.35 Å and the diffraction rings well-indexed to the fcc Au, respectively. Importantly, by comparing the grain size change of obtained n-Au materials and AuNPs-compact-28.2 GPa (Table 1), it could be found that no obvious grain growth occurred when compressing 4H Au NRBs under pressure while the grain size significantly increased after compressing the fcc Au NPs. These results indicated that the *in-situ* 4H-to-fcc phase transformation at high pressure could effectively inhibit the grain growth of Au and thus enable the preparation of n-Au materials. The inhibition of grain growth by phase transformation from 4H to fcc could be mainly attributed to the following reasons. First, during the compaction and cold forging, the 4H Au NRBs would experience severe plastic deformation and break into fragments with the original width. Simultaneously, the 4H phase started to transform to the fcc phase in which the diffusion coefficient of nucleated fcc nanocrystals would decrease under high pressure, resulting in the decreased crystal growth rate that would further refine the grains [37, 38]. Second, the continuous high pressure would promote the plastic deformation dominated by dislocation in the nanocrystals even after the 4H phase completely transformed to the fcc phase, which was also beneficial to the inhibition of grain growth [39, 40]. The polycrystalline Au compact prepared from the fcc Au foil at the pressure of 15.5 GPa, denoted as Au-foil-15.5 GPa, possessed a long strip-like microstructure with a width of ~ 350 nm and length of 0.4–1.5 μm (Fig. 3(j) and Table 1). The measured lattice distance of 2.35 Å in HRTEM images (Fig. 3(k) and the inset) and the diffraction spots in SAED pattern (Fig. 3(l)) of Au-foil-15.5 GPa further confirmed the fcc phase.

3.4 Mechanical properties of as-prepared n-Au materials

The hardness and compressive strength of the prepared n-Au materials were tested. The H_V values in Fig. 4(a) were calculated based on the equation of $H_V = 1{,}854.4\ F/L^2$, where F is the applied

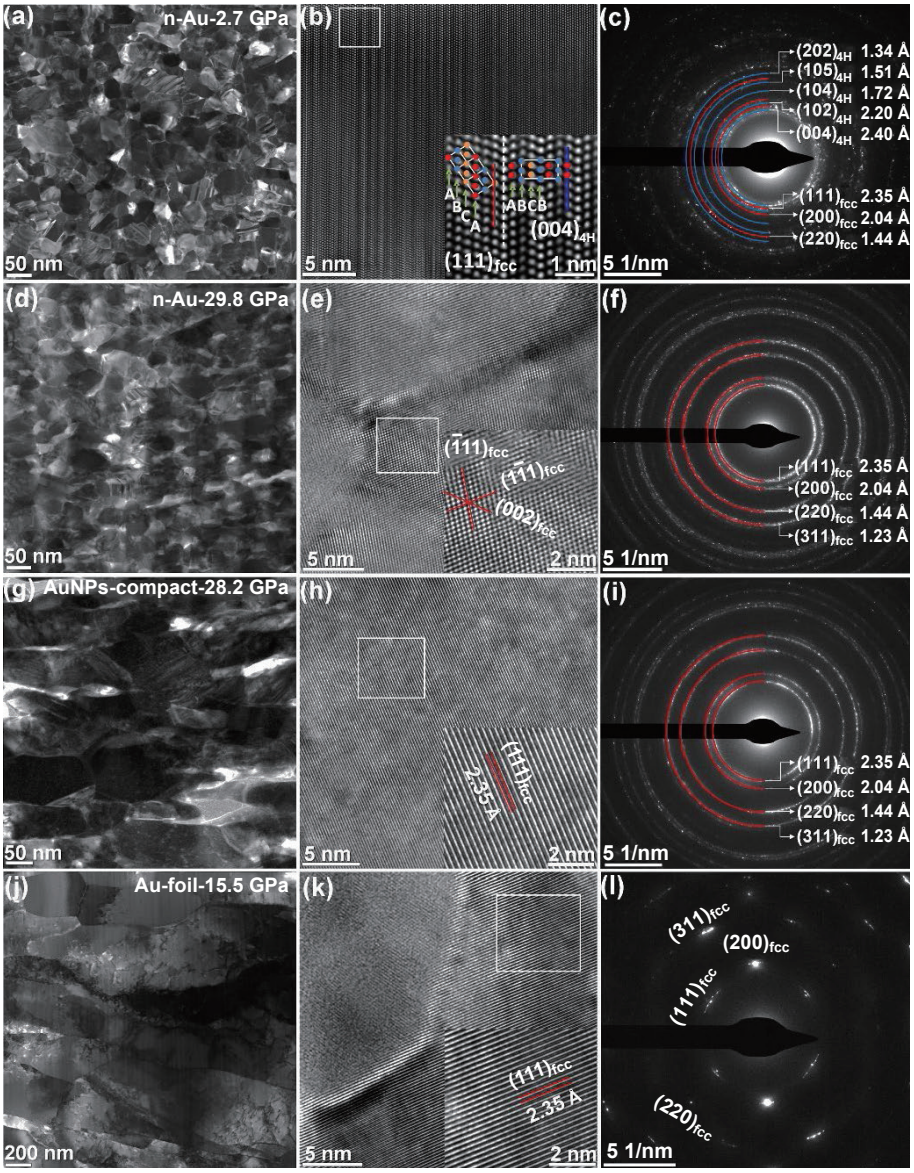

Figure 3 (a) Dark field TEM image, (b) HRTEM image, and (c) SAED pattern taken from the whole area in (a) of n-Au-2.7 GPa. (d) Dark field TEM image, (e) HRTEM image, and (f) SAED pattern taken from the whole area in (d) of n-Au-29.8 GPa. (g) Dark field TEM image, (h) HRTEM image, and (i) SAED pattern taken from the whole area in (g) of AuNPs-compact-28.2 GPa. (j) TEM image, (k) HRTEM image, and (l) SAED pattern taken from the whole area in (j) of Au-foil-15.5 GPa. Insets in (b), (e), (h), and (k): enlarged images taken from the corresponding white rectangles.

Table 1 The grain sizes of starting materials and Au samples obtained at different fabrication pressures

Starting material	Grain dimensions of starting material	Pressure of cold-forging	Grain dimensions of obtained Au sample
4H Au NRBs	36.2 ± 13.0 nm (width)	2.7 GPa	44.5 ± 11.2 nm
		8.5 GPa	42.7 ± 10.8 nm
		29.8 GPa	37.6 ± 8.4 nm
fcc Au NPs	64.7 ± 26.8 nm (size)	28.2 GPa	183.9 ± 54.7 nm (length) 96.6 ± 37.0 nm (width)
Au foil	~ 350 nm (width) 0.4–1.5 μm (length)	15.5 GPa	~ 350 nm (width) 0.4–1.5 μm (length)

load and L is the mean length of the two diagonals of the indentation (Fig. S6 in the ESM). It is found that a series of n-Au materials prepared under different pressures from 2.7 to 29.8 GPa showed similar H_V of 0.95 ± 0.08 GPa (Fig. 4(a)). Given that these n-Au materials had similar grain sizes of ~ 40 nm (Table 1) but different crystal phase compositions (Figs. 3(a)–3(f) and Fig. S4 in the ESM), it could be concluded that the hardness of prepared n-Au materials was mainly dependent on their grain sizes instead of their crystal phases, which was consistent with the classical Hall–Petch relationship [41]. In addition, the hardness of the aforementioned Au materials prepared by high-pressure cold-forging of other Au starting materials, including the fcc Au foil and Au NPs, was also investigated. The H_V of the original microcrystalline Au foil was only 0.45 GPa, which was comparable with that of the reported bulk Au (0.43 GPa) [42]. After the high-pressure cold-forging at different pressures, a series of obtained Au-foil-compacts showed significantly enhanced hardness of 0.73 ± 0.02 GPa (red solid squares in Fig. 4(a)). Such hardening effect through the high-pressure cold-forging was similar to the commonly reported cold working or strain hardening

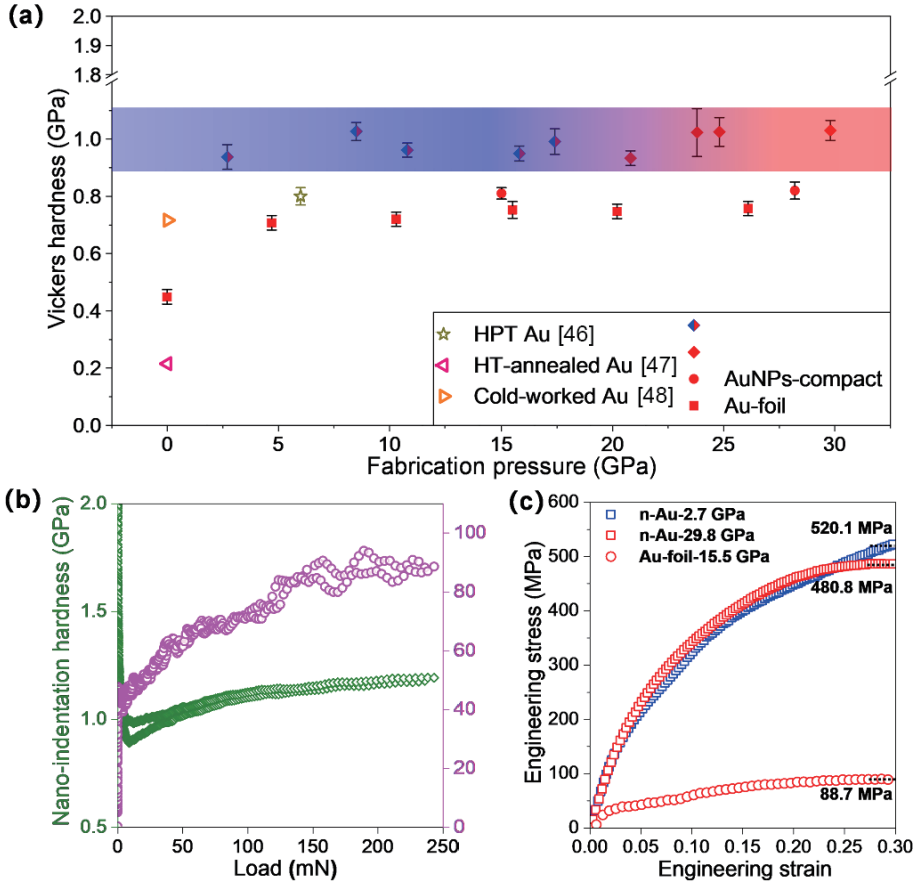

Figure 4 (a) The H_V of the n-Au materials prepared by high-pressure cold-forging of different Au starting materials at different pressures. Some previously reported representative Au materials, including HPT Au [46], HT-annealed Au [47], and cold-worked Au [48], are used as comparison. (b) Nano-indentation hardness and Young's modulus of n-Au-15.5 GPa. (c) Uniaxial compressive stress–strain curves of the micro-pillars prepared from n-Au-2.7 GPa, n-Au-29.8 GPa, and Au-foil-15.5 GPa.

effect [43–45]. Moreover, the AuNPs-compacts obtained via the high-pressure cold-forging of the fcc Au NPs at 15.0 and 28.2 GPa exhibited the similar hardness of 0.80 ± 0.02 GPa (red solid dots in Fig. 4(a)). Based on the aforementioned results, the n-Au materials prepared from the 4H Au NRBs showed higher H_V as compared with those prepared by using fcc Au foil and Au NPs as starting materials. Excitingly, compared with the previously reported Au materials prepared by other methods, including high-pressure torsion (HPT) [46], high-temperature (HT) annealing [47], and cold working [48], the hardness of our prepared n-Au materials was among the best (Fig. 4(a)).

The nano-indentation hardness (H_n) and Young's modulus (E) of a representative n-Au material prepared at 15.5 GPa, i.e., n-Au-15.5 GPa, were also measured via the CSM technique (Fig. 4(b) and Fig. S7 in the ESM). The convergent H_n of n-Au-15.5 GPa reached ~ 1.2 GPa, and the convergent E of n-Au-15.5 GPa was measured to be 88.2 GPa (Fig. 4(b)), which was higher than the reported microcrystalline fcc Au (79 GPa) [11], indicating the better mechanical property of our prepared n-Au material.

Moreover, the compressive yield strength of the as-synthesized Au materials was also tested. As illustrated in Fig. 4(c) and Fig. S8 in the ESM, the n-Au-2.7 GPa with the mixed 4H/fcc phases showed a compressive yield strength of 125.1 MPa, and the n-Au-29.8 GPa with the pure fcc phase showed a compressive yield strength of 140.2 MPa, which was ~ 4.2 times of Au-foil-15.5 GPa (33.4 MPa) and ~ 3.1 times of the reported single-crystal Au micro-pillars (45 MPa) [49]. At the strain of 0.3, the obtained n-Au-2.7 GPa and n-Au-29.8 GPa samples could bear the stress of 520.1 and 480.8 MPa, respectively, while the Au-foil-15.5 GPa could only bear the stress of 88.7 MPa (Fig. 4(c)). The measured hardness and compressive strength demonstrated the superior mechanical performance of our prepared n-Au materials, revealing the importance of starting nanomaterials in the high-pressure cold-forging for the preparation of hard n-Au materials.

4 Conclusion

In summary, the n-Au materials with the grain size of ~ 40 nm have been prepared via the high-pressure cold-forging of the unconventional 4H Au NRBs. It is found that the *in-situ* 4H-to-fcc phase transformation during the high-pressure cold-forging could effectively inhibit the grain growth in the obtained n-Au materials. As a result, the as-prepared n-Au materials exhibited significantly enhanced H_V and compressive yield strength, which were about 2.2 and 4.2 times of microcrystalline Au foil, respectively. Such high hardness of our n-Au materials was among the best of the reported Au materials. This work demonstrates that the combination of high-pressure fabrication and PEN is a promising strategy for the preparation of the novel nanocrystalline metals with superior mechanical properties.

Acknowledgements

This work was supported by the National Natural Science Foundation of China (Nos. 52090020, 51722209, and 51525205), and the National Key Research and Development Program of China (No. 2018YFA0305900). Z. S. Z. acknowledges the NSF for Distinguished Young Scholars of Hebei Province of China (No. E2018203349), and M. D. M. acknowledges the China Postdoctoral Science Foundation (No. 2021M691051). Z. X. F. and H. Z. thank the support from ITC via Hong Kong Branch of National Precious Metals Material Engineering Research Center (NPMM), the Start-Up Grants (Nos. 9380100, 9610480, and

7200651), and grants (Nos. 9610478, 1886921, 7020013, and 7005512) from City University of Hong Kong.

Electronic Supplementary Material: Supplementary material (chemicals, sample preparation methods, characterizations, and additional figures) is available in the online version of this article at https://doi.org/10.1007/s12274-022-4226-5.

References

[1] Cantwell, P. R.; Tang, M.; Dillon, S. J.; Luo, J.; Rohrer, G. S.; Harmer, M. P. Grain boundary complexions. *Acta Mater.* **2014**, *62*, 1–48.

[2] Sun, L. G.; Wu, G.; Wang, Q.; Lu, J. Nanostructural metallic materials: Structures and mechanical properties. *Mater. Today* **2020**, *38*, 114–135.

[3] Van Swygenhoven, H.; Weertman, J. R. Deformation in nanocrystalline metals. *Mater. Today* **2006**, *9*, 24–31.

[4] Kumar, K. S.; Van Swygenhoven, H.; Suresh, S. Mechanical behavior of nanocrystalline metals and alloys. *Acta Mater.* **2003**, *51*, 5743–5774.

[5] Erb, U.; Palumbo, G.; McCrea, J. L. The processing of bulk nanocrystalline metals and alloys by electrodeposition. In *Nanostructured Metals and Alloys*; Whang, S. H., Ed.; Oxford: Woodhead Publishing Limited, 2011; pp 118–151.

[6] Dao, M.; Lu, L.; Asaro, R. J.; De Hosson, J. T. M.; Ma, E. Toward a quantitative understanding of mechanical behavior of nanocrystalline metals. *Acta Mater.* **2007**, *55*, 4041–4065.

[7] Fang, Z. Z.; Paramore, J. D.; Sun, P.; Chandran, K. S. R.; Zhang, Y.; Xia, Y.; Cao, F.; Koopman, M.; Free, M. Powder metallurgy of titanium-past, present, and future. *Int. Mater. Rev.* **2018**, *63*, 407–459.

[8] Segal, V. M. Engineering and commercialization of equal channel angular extrusion (ECAE). *Mater. Sci. Eng. A* **2004**, *386*, 269–276.

[9] Lu, L.; Shen, Y. F.; Chen, X. H.; Qian, L. H.; Lu, K. Ultrahigh strength and high electrical conductivity in copper. *Science* **2004**, *304*, 422–426.

[10] Okuda, S.; Tang, F. Thermal stability of nanocrystalline gold prepared by gas deposition method. *Nanostruct. Mater.* **1995**, *6*, 585–588.

[11] Sakai, S.; Tanimoto, H.; Mizubayashi, H. Mechanical behavior of high-density nanocrystalline gold prepared by gas deposition method. *Acta Mater.* **1998**, *47*, 211–217.

[12] Tanimoto, H.; Fujita, H.; Mizubayashi, H.; Sasaki, Y.; Kita, E.; Okuda, S. AFM observation of nanocrystalline Au prepared by a gas deposition method. *Mater. Sci. Eng. A* **1996**, *217−218*, 108–111.

[13] Chen, C. Y.; Yoshiba, M.; Nagoshi, T.; Chang, T. F. M.; Yamane, D.; Machida, K.; Masu, K.; Sone, M. Pulse electroplating of ultra-fine grained Au films with high compressive strength. *Electrochem. Commun.* **2016**, *67*, 51–54.

[14] Tian, Y. J.; Xu, B.; Yu, D. L.; Ma, Y. M.; Wang, Y. B.; Jiang, Y. B.; Hu, W. T.; Tang, C. C.; Gao, Y. F.; Luo, K. et al. Ultrahard nanotwinned cubic boron nitride. *Nature* **2013**, *493*, 385–388.

[15] Huang, Q. Yu, D. L.; Xu, B.; Hu, W. T.; Ma, Y. M.; Wang, Y. B.; Zhao, Z. S.; Wen, B.; He, J. L.; Liu, Z. Y. et al. Nanotwinned diamond with unprecedented hardness and stability. *Nature* **2014**, *510*, 250–253.

[16] Shi, Y. F.; Lyu, Z.; Zhao, M.; Chen, R. H.; Nguyen, Q. N.; Xia, Y. N. Noble-metal nanocrystals with controlled shapes for catalytic and electrocatalytic applications. *Chem. Rev.* **2021**, *121*, 649–735.

[17] Lu, S. Y.; Liang, J. Z.; Long, H. W.; Li, H. X.; Zhou, X. C.; He, Z.; Chen, Y.; Sun, H. Y.; Fan, Z. X; Zhang, H. Crystal phase control of gold nanomaterials by wet-chemical synthesis. *Acc. Chem. Res.* **2020**, *53*, 2106–2118.

[18] Fan, Z. X.; Huang, X.; Chen, Y.; Huang, W.; Zhang, H. Facile synthesis of gold nanomaterials with unusual crystal structures. *Nat. Protoc.* **2017**, *12*, 2367–2376.

[19] Zhang, Y.; Hu, B.; Cao, X. M.; Luo, L.; Xiong, Y.; Wang, Z. P.; Hong, X.; Ding, S. Y. β-Cyclodextrin polymer networks stabilized gold nanoparticle with superior catalytic activities. *Nano Res.* **2021**, *14*, 1018–1025.

[20] Ding, S. J.; Ma, L.; Feng, J. R.; Chen, Y. L.; Yang, D. J.; Wang, Q. Q. Surface-roughness-adjustable Au nanorods with strong plasmon absorption and abundant hotspots for improved SERS and photothermal performances. *Nano Res.* **2022**, *15*, 2715–2721.

[21] Yan, X. N.; Chen, Q.; Song, Q.; Huo, Z. Y.; Zhang, N.; Ma, M. M. Continuous mechanical tuning of plasmonic nanoassemblies for tunable and selective SERS platforms. *Nano Res.* **2021**, *14*, 275–284.

[22] Chen, Y.; Lai, Z. C.; Zhang, X.; Fan, Z. X.; He, Q. Y.; Tan, C. L.; Zhang, H. Phase engineering of nanomaterials. *Nat. Rev. Chem.* **2020**, *4*, 243–256.

[23] Ge, Y. Y.; Shi, Z. Y.; Tan, C. L.; Chen, Y.; Cheng, H. F.; He, Q. Y.; Zhang, H. Two-dimensional nanomaterials with unconventional phases. *Chem* **2020**, *6*, 1237–1253.

[24] Liu, J. W.; Huang, J. T.; Niu, W. X.; Tan, C. L.; Zhang, H. Unconventional-phase crystalline materials constructed from multiscale building blocks. *Chem. Rev.* **2021**, *121*, 5830–5888.

[25] Liang, J. Z.; Ge, Y. Y.; He, Z.; Yun, Q. B.; Liu, G. G.; Lu, S. Y.; Zhai, L.; Huang, B.; Zhang, H. Wet-chemical synthesis and applications of amorphous metal-containing nanomaterials. *Nano Res.* in press, https://doi.org/10.1007/s12274-021-4007-6.

[26] Sheng, B. B.; Cao, D. F.; Shou, H. W.; Moses, O. A.; Xu, W. J.; Xia, Y. J.; Zhou, Y. Z.; Wang, H. J.; Wan, P.; Zhu, S. et al. Support induced phase engineering toward superior electrocatalyst. *Nano Res.* **2022**, *15*, 1831–1837.

[27] Fan, Z. X.; Bosman, M.; Huang, X.; Huang, D.; Yu, Y.; Ong, K. P.; Akimov, Y. A.; Wu, L.; Li, B.; Wu, J. et al. Stabilization of 4H hexagonal phase in gold nanoribbons. *Nat. Commun.* **2015**, *6*, 7684.

[28] Huang, X.; Li, S. Z.; Huang, Y. Z.; Wu, S. X.; Zhou, X. Z.; Li, S. Z.; Gan, C. L.; Boey, F.; Mirkin, C. A.; Zhang, H. Synthesis of hexagonal close-packed gold nanostructures. *Nat. Commun.* **2011**, *2*, 292.

[29] Lu, X. M.; Tuan, H. Y.; Korgel, B. A.; Xia, Y. N. Facile synthesis of gold nanoparticles with narrow size distribution by using AuCl or AuBr as the precursor. *Chem.—Eur. J.* **2008**, *14*, 1584–1591.

[30] Mao, H. K.; Xu, J.; Bell, P. M. Calibration of the ruby pressure gauge to 800 kbar under quasi-hydrostatic conditions. *J. Geophys. Res. Solid Earth* **1986**, *91*, 4673–4676.

[31] Hammersley, A. P.; Svensson, S. O.; Hanfland, M.; Fitch, A. N.; Hausermann, D. Two-dimensional detector software: From real detector to idealised image or two-theta scan. *High Press. Res.* **1996**, *14*, 235–248.

[32] Toby, B. H.; Von Dreele, R. B. GSAS-II: The genesis of a modern open-source all purpose crystallography software package. *J. Appl. Crystall.* **2013**, *46*, 544–549.

[33] Li, Q.; Niu, W. X.; Liu, X. C.; Chen, Y.; Wu, X. T.; Wen, X. D.; Wang, Z. W.; Zhang, H.; Quan, Z. W. Pressure-induced phase engineering of gold nanostructures. *J. Am. Chem. Soc.* **2018**, *140*, 15783–15790.

[34] Li, P. F.; Han, Y.; Zhou, X.; Fan, Z. X.; Xu, S.; Cao, K.; Meng, F. L.; Gao, L. B.; Song, J.; Zhang, H. et al. Thermal effect and Rayleigh instability of ultrathin 4H hexagonal gold nanoribbons. *Matter* **2020**, *2*, 658–665.

[35] Birch, F. Finite strain isotherm and velocities for single-crystal and polycrystalline NaCl at high pressures and 300 K. *Geophys. Res. Solid Earth* **1978**, *83*, 1257–1268.

[36] Shim, S. H.; Duffy, T. S.; Takemura, K. Equation of state of gold and its application to the phase boundaries near 660 km depth in Earth's mantle. *Earth Planet. Sci. Lett.* **2002**, *203*, 729–739.

[37] Ma, P.; Zou, C. M.; Wang, H. W.; Scudino, S.; Fu, B. G.; Wei, Z. J.; Kühn, U.; Eckert, J. Effects of high pressure and SiC content on microstructure and precipitation kinetics of Al-20Si alloy. *J. Alloys Compd.* **2014**, *586*, 639–644.

[38] Wang, H. W.; Zhu, D. D.; Zou, C. M.; Wei, Z. J. Evolution of the microstructure and nanohardness of Ti-48 at.% Al alloy solidified under high pressure. *Mater. Des.* **2012**, *34*, 488–493.

[39] Chen, B.; Lutker, K.; Raju, S. V.; Yan, J. Y.; Kanitpanyacharoen, W.; Lei, J. L.; Yang, S. Z.; Wenk, H. R.; Mao, H. K.; Williams, Q. Texture of nanocrystalline nickel: Probing the lower size limit of dislocation activity. *Science* **2012**, *338*, 1448–1451.

[40] Zhou, X. L.; Feng, Z. Q.; Zhu, L. L.; Xu, J. N.; Miyagi, L.; Dong, H. L.; Sheng, H. W.; Wang, Y. J.; Li, Q.; Ma, Y. M. et al. High-

pressure strengthening in ultrafine-grained metals. *Nature* **2020**, *579*, 67–72.

[41] Weertman, J. R. Hall−Petch strengthening in nanocrystalline metals. *Mater. Sci. Eng. A* **1993**, *166*, 161–167.

[42] Newby, J. *Metals Handbook, Volume 8: Mechanical Testing,* 9th ed.; ASM International: Materials Park, 1985.

[43] Mecking, H.; Kocks, U. F. Kinetics of flow and strain-hardening. *Acta Metall.* **1981**, *29*, 1865–1875.

[44] Poniatowski, M.; Clasing, M. Dispersion hardened gold. *Gold Bull.* **1972**, *5*, 34–36.

[45] Gupta, R. K.; Kumar, V. A.; Mathew, C.; Rao, G. S. Strain hardening of titanium alloy Ti6Al4V sheets with prior heat treatment and cold working. *Mater. Sci. Eng. A* **2016**, *662*, 537–550.

[46] Edalati, K.; Horita, Z. High-pressure torsion of pure metals: Influence of atomic bond parameters and stacking fault energy on grain size and correlation with hardness. *Acta Mater.* **2011**, *59*, 6831–6836.

[47] Grimwade, M. The metallurgy of gold. Interdiscip. *Sci. Rev* **1992**, *17*, 371–381.

[48] Du Toit, M.; Van Der Lingen, E.; Glaner, L.; Süss, R. The development of a novel gold alloy with 995 fineness and increased hardness. *Gold Bull.* **2002**, *35*, 46–52.

[49] Greer, J. R.; Oliver, W. C.; Nix, W. D. Size dependence of mechanical properties of gold at the micron scale in the absence of strain gradients. *Acta Mater.* **2005**, *53*, 1821–1830.